

Segmentation of human brain using structural MRI

Gunther Helms¹ 

Received: 10 July 2015 / Revised: 27 November 2015 / Accepted: 1 December 2015 / Published online: 6 January 2016
© ESMRMB 2015

Abstract Segmentation of human brain using structural MRI is a key step of processing in imaging neuroscience. The methods have undergone a rapid development in the past two decades and are now widely available. This non-technical review aims at providing an overview and basic understanding of the most common software. Starting with the basis of structural MRI contrast in brain and imaging protocols, the concepts of voxel-based and surface-based segmentation are discussed. Special emphasis is given to the typical contrast features and morphological constraints of cortical and sub-cortical grey matter. In addition to the use for voxel-based morphometry, basic applications in quantitative MRI, cortical thickness estimations, and atrophy measurements as well as assignment of cortical regions and deep brain nuclei are briefly discussed. Finally, some fields for clinical applications are given.

Keywords Brain · Segmentation · MRI · Morphometry · Cortical thickness

Introduction

The progress of magnetic resonance imaging (MRI) has naturally driven the development of image processing for segmentation of tissue—especially of the brain [1]. Here, the widespread interest in studying individual morphology has been met by methodological advantages, such as non-invasiveness, high intrinsic contrast and resolution, and the

rigid encasing in the skull. Digital image segmentation, that is, the automated partitioning of a 2D image or 3D image volume into clusters or tissue “classes”, namely grey matter (GM), white matter (WM), and cerebrospinal fluid (CSF) is the key step for further analysis and display.

After the advent of three-dimensional (3D), high-contrast, high-resolution structural MRI, the key concepts and methods of brain segmentation were developed in a span of a few years around the shift of the millennium [2]. Automated tools for segmentation are provided with the standard software packages for brain image processing such as “Statistical Parametric Mapping” (SPM, Wellcome Trust Centre for Neuroimaging, London, UK; www.fil.ion.ucl.ac.uk/spm) or FSL (FMRIB software library, Centre for Functional MRI of the Brain, Oxford, UK; www.fmrib.ox.ac.uk/fsl). The most common tool for surface-based segmentation is FreeSurfer (Harvard University, Cambridge, MA, USA; surfer.nmr.mgh.harvard.edu). More recently, the TOADS-CRUISE brain segmentation tools (John Hopkins University, Baltimore, MD, USA www.nitrc.org/toads-cruise) were developed using the Java Image Science Toolkit (JIST) [3] as plug-ins for the MIPAV platform (Medical Image Processing, Analysis, and Visualization; mipav.cit.nih.gov). Another open-source platform with plug-in capability is 3D Slicer (www.slicer.org) [4] and the “Insight Segmentation and Registration Toolkit” (ITK) of the National Library of Medicine (www.itk.org). The methods for brain segmentation are still under development towards integration of processing steps, automation, and handling of large cohorts. The Java Image Science Toolkit (JIST) has been designed to be a development tool for all operative systems, but also the Matlab-based SPM is open for extensions.

The latest versions of a wide range of publicly available software can be accessed via the “NeuroInformatic Tools and Resources Clearinghouse” (NITRC; www.nitrc.org).

✉ Gunther Helms
gunther.helms@med.lu.se

¹ Medical Radiation Physics, Lund University Hospital, Barngatan 2B, 221 85 Lund, Sweden

To name a few others: UCLA's Brain Suite (brainsuite.org), the "Computational Morphometry Toolkit" (CMTK), the segmentation package of the Universities of North Carolina Utah "Atlas Based Classification" (ABC), and the toolbox of the University of North Carolina, Chapel Hill, NC, USA (www.med.unc.edu/bric/ideagroup/free-softwares). These often specialize in specific high end applications, but do also offer basic functionalities of linear and non-linear image registration, brain extraction, pixel-wise and surface segmentation, which will be discussed below. Important to the prospective user, the website features also links to references and "reviews", that is, papers on systematic comparisons between different tools. Software is available to compare results from individuals or algorithms [Simultaneous Truth and Performance Level Estimation (STAPLE) www.crl.med.harvard.edu/software/CRKIT/index.php] [5].

This non-technical review comprises the main aspects of the structural MRI contrast in the context of human neuroanatomy and segmentation software. Techniques based on diffusion MRI and fiber tracking are not covered. The focus is on the freely available and thus most widely used software packages mentioned above. These have been ever increasingly used to study healthy brain development and aging, as well as in countless clinical studies. The focus of the latter is finding biomarkers for neurodegeneration and treatment trials reflecting volumetric, morphological, or surface features. Arguably, image segmentation is the stepping stone for advanced methods in image-based neuroscience, in particular in computational neuroanatomy. Three-dimensional population-based atlases have been integrated with the segmentation to assign cortical regions and deep brain nuclei. The aim is to detect ever smaller structures as in cortical profiles and the integration of MRI with histology and other imaging modalities.

Structural MRI contrast

The undisputed main source of MRI contrast between GM and WM is myelin, the multi-lamellar wrapping around axons that increases the velocity of far-reaching neuronal communication. Myelin forms a highly ordered ultrastructural environment that decreases T1, T2, and proton density (PD) by cross-relaxation of rotationally free water and the immobile macromolecules in phospholipid-bilayers and embedded proteins [6]. Since T1 is mainly determined by the relation of water content to structural material [7], "structural MRI" is often used synonymously with T1-weighted MRI. The second source is the presence of paramagnetic iron throughout the brain. It is most efficient in shortening T2* and T2, but also T1 [8, 9] when stored as super-paramagnetic ferritin, a globular protein structure that can store up to 4500 Fe³⁺ ions. Highest

iron concentrations are found in the deep brain nuclei/basal ganglia increasing with age [10]. Myelin content and axonal density are also the basis for intracortical contrast as well as for contrast gradients in some deep brain nuclei. An excess of free water in the extracellular space, e.g., in perivascular Virchow-Robin spaces, oedema, or vascular lesions, increases T2 and T2* more strongly than T1 and is thus best seen on T2-weighted MRI against the background of WM. The connective tissue of the dura mater has short T2 and T2* and appears dark at sufficiently long echo times, as do larger vessels [11].

The methods of choice for structural MRI are T1-weighted high-resolution 3D sequences, e.g. MP-RAGE (magnetization-prepared rapid acquisition of gradient echoes) or MDEFT (modified driven equilibrium Fourier transform), which have been optimized for GM-WM-CSF contrast [12–14]. Head coils with multiple (8–64) surface elements to receive the radio frequency signal yield sufficient signal-to-noise at an isotropic resolution of typically 1 mm (or below) within 5–12 min at 3 Tesla field strength.

In most brain regions, GM and WM are characterized by similar properties. Particularly in the cerebrum, T1-weighted GM-WM contrast exceeds the contrast within the cortex and myelinated WM. Important exceptions are discussed below, where GM is affected by differences in axonal density in and iron content and WM by axonal diameter, coherence, and density. Because of the short echo-times of 5 ms or below, connective tissue and venous blood in the large draining sinuses appear at signal levels similar to grey matter and so do the muscles. Bright signals of subcutaneous fat should be suppressed or prevented to be shifted toward the brain by strength and polarity of the read-out gradient.

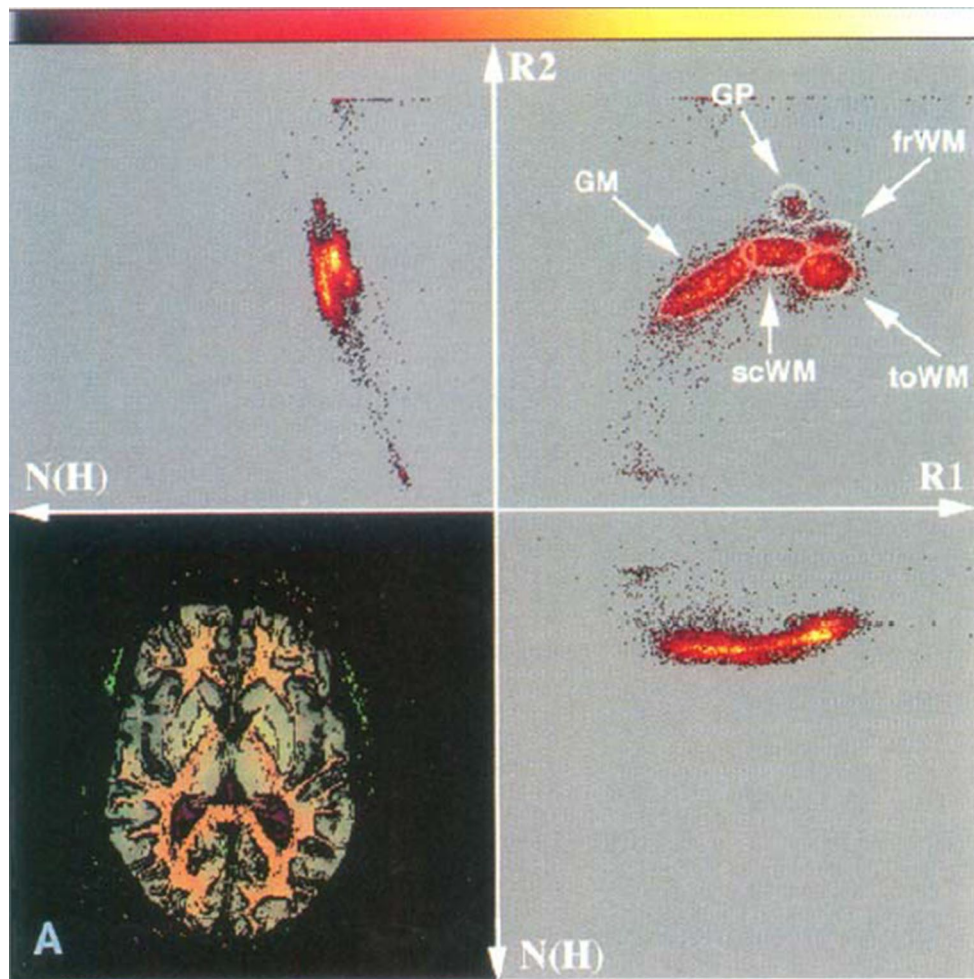
The intra-class homogeneity in GM and WM known from clinical MR systems can no longer be taken for granted at 7T due to high spatial resolution (down to 0.35 mm) and the influence of static field effects. A dedicated toolbox has been developed at the Max-Planck Institute for Human Cognitive and Brain Sciences (MPICBS), Leipzig. CBS High-Res Brain Processing Tools (CHB, www.cbs.mpg.de/institute/software/cbs-hrt/download.html) are released as plug-ins for the MIPAV software package.

Voxel-based segmentation

Voxel-by-voxel segmentation, the fundamental and most common approach, is based on the local signal level in the context of the signal distribution as depicted in a histogram plot. The underlying assumption is that GM, WM, and CSF exhibit specific distributions of signal levels and tissue properties that, nevertheless, may overlap.

Some early strategies for brain segmentation were based on maps of MR parameters, e.g. T1, T2, and PD [15]. Historically,

Fig. 1 Segmentation by tissue properties. Segmented image and colour-coded 2D histograms of PD ($N(H)$), $R1 = 1/T1$ and $R2 = 1/T2$ (from [12], reproduced with permission). MR parameters were derived from spin-echo MRI. In the $R1-R2$ histogram, note the distinctly faster relaxation in the iron-rich deep brain nuclei (globus pallidus, GP) overlapping with WM in T1. Note also that the large GM cluster extends into the subcortical (scWM) region. From [15]



this approach was the immediate conclusion from the fundamental paradigm of early MRI, namely that a tissue can be characterized by these parameters. Such maps can be derived from conventional spin echo MRI, are reproducible within error and providing a high contrast and good separation of clusters (Fig. 1). Dividing the parameter space into a predefined separate regions leads to segmentation into discrete classes.

The MRI signal, however, is subject to arbitrary scaling and to spatial weighting by the local sensitivity of the receive coil. This “bias field” is smooth compared to the cortical structures, but poorly reproducible as it obviously depends on the positioning of the skull in the receive coil. Thus, the bias field has to be estimated individually and removed by pre-processing the data. Such efforts were undertaken to ensure the comparability of longitudinal MR studies. The N3 algorithm [16] has found widespread use for bias removal before this step was integrated into standard segmentation software. Here, the spatial frequency or “flexibility” of the bias field is controlled by the width of a Gaussian kernel. A more recent variant is N4ITK [17].

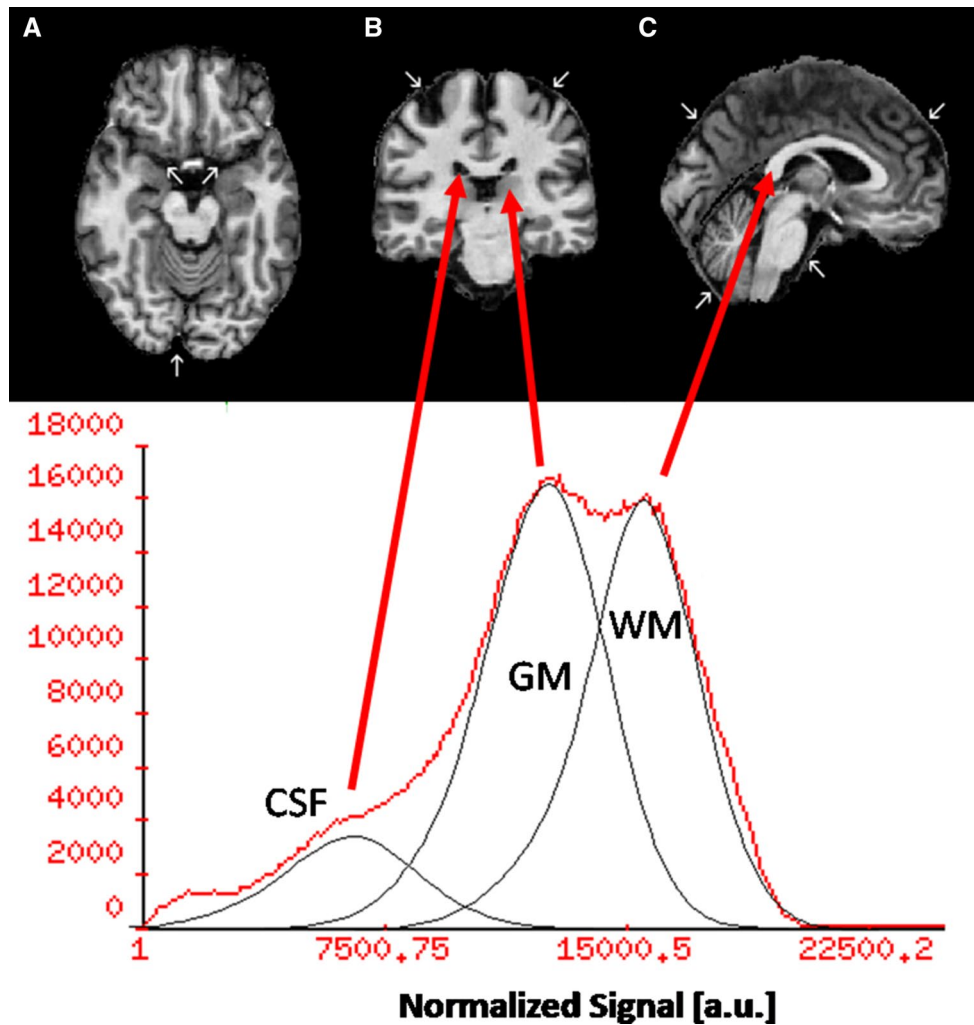
The signal from “non-brain” voxels complicate the analysis, as these may represent a variety of tissues of muscle,

bone, major arteries, connective tissue, mucosa, eyes, subcutaneous, and retro-bulbar fat. Such signals can overlap with the brain intensities (muscle) or be extremely hyperintense (fat and arteries on T1-w MRI and eyes on T2-w MRI) especially when exposed to severe signal bias. The classification and bias correction is greatly simplified by removing such pixels.

The FAST algorithm of FSL (FMRIBs advanced segmentation tool) [18] works on the extracted brain. The extra-dural voxels are then removed by a brain mask (“skull stripping”). FSL’s brain extraction tool (BET) identifies the drop of signal at the brain boundary by a locally growing or contracting sphere [19]. There are numerous methods for skull stripping; a comparison of some is given in [20]. Though BET is still widely used, hybrid methods such as “Robust Brain Extraction” (ROBEX, www.nitrc.org/projects/robex) [21], or the “Simple Paradigm for Extra-Cerebral tissue Removal” (SPECTRE, part of the TOADS-package) [22], or the BrainMask volume processing tool (www.nitrc.org/projects/brainmask) [23] are becoming increasingly popular because these adhere better to the cortical surface.

Fig. 2 Gaussian mixture model.

As the starting point for voxel-based segmentation, the histogram of T1-weighted intensities is approximated by a superposition of Gaussian functions. This assignment of tissue probabilities is sensitive to noise as it does not use spatial information (modified FSL course material www.fmrib.ox.ac.uk/fsl)



To illustrate the segmentation problem in the presence of noise, Fig. 2 shows a typical overlapping signal distribution across subdural space after bias correction. The intensity histogram is approximated by a superposition of three normal distributions (finite Gaussian mixture model) each representing a tissue class. Pixels showing intensities without overlap can be reliably assigned to one tissue class (that is, bright to WM and dark to CSF). The other pixels are assigned probabilities to belong to each according to the relative contribution of the Gaussian distribution (e.g. 30 % GM and 70 % CSF at an intensity of 7500 a.u.). This assignment, however, does not make use of spatial information and is sensitive to noise: pixels of intensity 7500 will be scattered about CSF and GM subspaces.

FAST uses a discrete Markov random field to obtain prior spatial information and then iteratively updates the assignment to the correct class (Fig. 3). For example, a pixel of low likelihood for GM can be assigned with an increased posterior probability to that class if surrounded by GM pixels. FAST is designed to be robust against low

SNR of the segmented image; for details see [18] and for the Bayesian approach [24].

The ever refined approach of SPM (in various versions of SPM and toolboxes) applies a Bayesian model using spatial maps of prior information for each class based on a large cohort of healthy subjects [25]. Hence, registration (or normalization) to an image template defining a standard for a 3D stereotactic space becomes prerequisite of the segmentation and was finally integrated into the process of unified segmentation [26]. This prior spatial information for each class is in the form of probability images—provided by the Montreal Neurological Institute (MNI)—which have been constructed from the MR images of 152 subjects (66 women and 86 men; ages between 18 and 44 years, with a mean age of 25 years) [27]. To illustrate the effect of affine versus locally non-linear spatial transformations, Fig. 4 shows two averaged templates of the MNI that are used with both FSL and SPM. Note that the MNI templates are considerably larger than a normal head, especially in the left-right (x) dimension. The horizontal plane

Fig. 3 Voxel-based segmentation. Voxel-based segmentation of 3D structural MRI (*lower left*) in a healthy subject using FAST. The 1 mm voxels are coded by the dominant tissue class (>0.5 probability): GM = red, WM = yellow, CSF = blue, non-brain = green [11]. The arrows point to misassigned non-brain

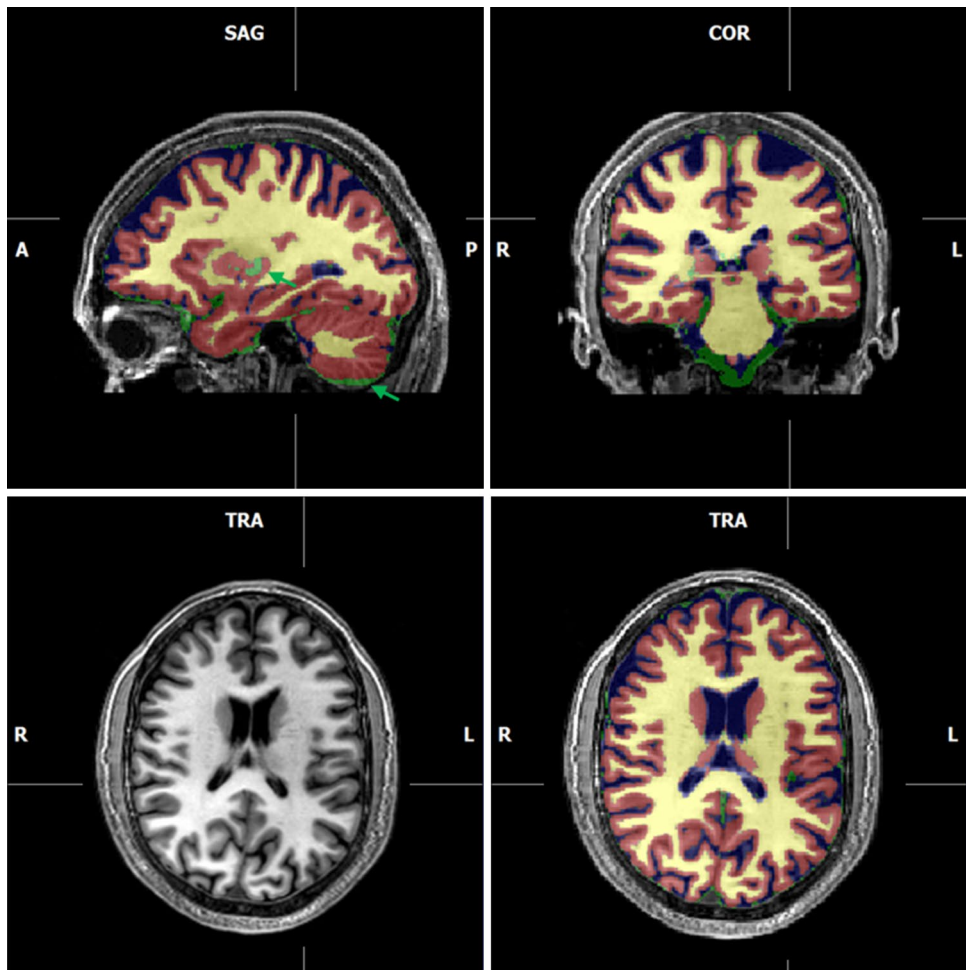
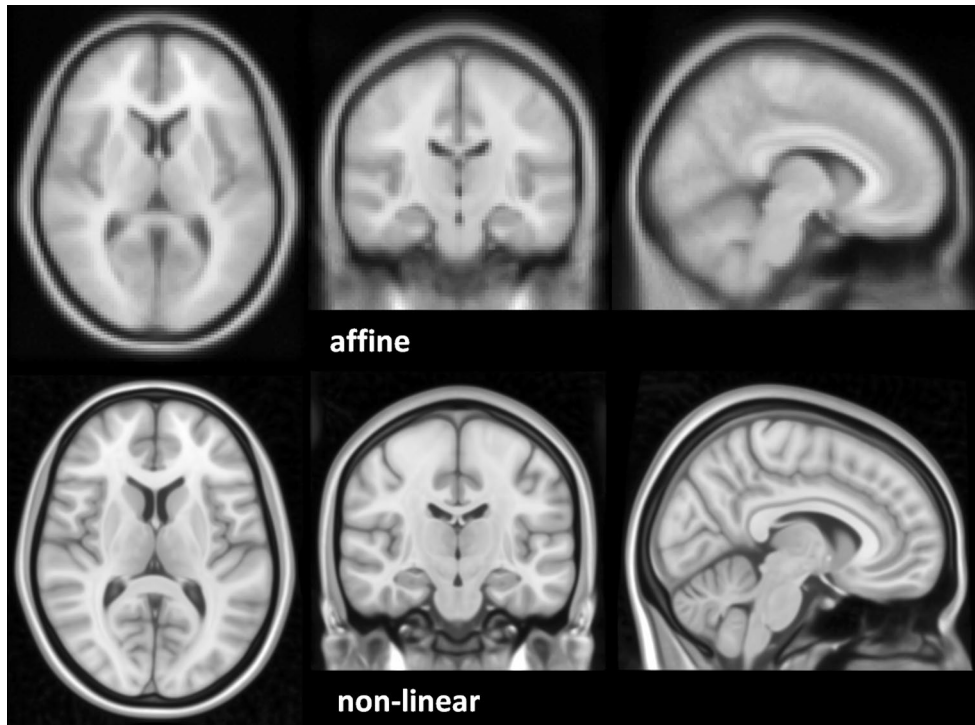


Fig. 4 Multi-subject averaging in stereotactic space. Shown are the MNI templates from 152 healthy subjects [27] as used by SPM and FSL. The top row shows the results after affine spatial transformation (12 parameters for shift, rotation, scaling, and skewing). The blurring of the cortical areas reflects the variation of gyration. In contrast, the deep brain structures show much less morphological variation. With non-linear registration (bottom row), a reduced degree of blurring can be chosen until—in the extreme—the individual morphology of the source data disappears. The morphological information is then transferred to the deformation field



deviates by about 7° from the inter-commissural orientation that is commonly used in neuroradiology.

Efforts are being made to improve the prior probability maps as these influence the estimated posterior probability maps, especially in the thalamus and basal ganglia. The construction of appropriate priors is also recommended when applying SPM to developing and aging brains or in neurodegeneration [26]. FSL's FAST can be readily applied up to four channels without priors, but may lead to misclassification where contrast is poor. Also, ABC (3D Slicer) performs atlas-based segmentation of brain tissue and CSF on co-registered input modalities [28].

Voxel-based morphometry

The maps of GM probability from the segmentation can be used to test for morphological differences between cohorts. In voxel-based morphometry (VBM), a statistical comparison of local GM volume is performed in standard stereotactic space, e.g., that defined by the MNI template. Since the registration of the individual brains to standard space involves scaling of volume, the corresponding factors are multiplied (“modulated”) upon the probability maps, turning these into estimates of partial GM volume. When using nonlinear spatial normalization, the volumes of certain brain regions will grow, whereas others will shrink. Local scaling factors are determined by the Jacobian matrix in nonlinear registration models. Since the WM of the centrum semiovale forms a compact spatial volume, local deformation of WM partial volume can be unreliable. Then, convolution of the “spatially normalized” and “modulated” partial volume maps with a 3D Gaussian kernel of typically 6–10 mm width combines of the mean amount of surrounding GM into each pixel. These smoothed maps are finally compared between cohorts by the standard methods of statistical mapping. Clusters of significant changes are often displayed a projections with the outlines of the brain (“glass brain”) or as maps onto the rendered surface brain.

VBM has become the most common approach for clinical morphological studies, since it is very sensitive, does not put high demands on data acquisition. From a historical perspective, VBM has been available for a long time as part of the SPM software [2]. One of the highlights of VBM application was the detection of training-induced increased of cortical GM [29], but the underlying mechanisms are still subject to debate. Note that cohort-based statistical analysis using voxel-based morphometry (VBM) is highly sensitive and may be influenced by the scanner and receive coil [30].

Number of tissue classes

The brain is commonly segmented into three classes of GM, WM, and CSF, but more classes, e.g. of lesions, can be desired. For intensity-based algorithms, however, each class must be supported by a Gaussian mode at characteristic signal level. This information can be obtained from a co-localized volume exhibiting a different contrast as it is normally not provided by T1-weighted MRI. For multi-spectral segmentation in a multi-dimensional feature space, each class is represented by a multi-dimensional Gaussian distribution that may overlap except in one dimension. In Fig. 3, non-brain voxels containing larger vessels and the dura mater can be identified by their low intensity on 3D turbo spin-echo (TSE) data [11]. For advanced segmentation problems, like of midbrain and brainstem [31], multi-spectral quantitative maps are increasingly used.

In addition to information from intensity and spatial priors, topologic criteria have been included [32]. The Topology-Preserving Anatomy-Driven Segmentation algorithm (TOADS, MIPAV/JIST platform) specifically addresses cerebral and cerebellar hemispheres, ventricular and sulcal CSF, putamen, caudate, thalamus, and brainstem [33]. The segmentation problem stated above is thus gradually shifted towards identifying subregions of an “atlas” based on intensity and topology (see below).

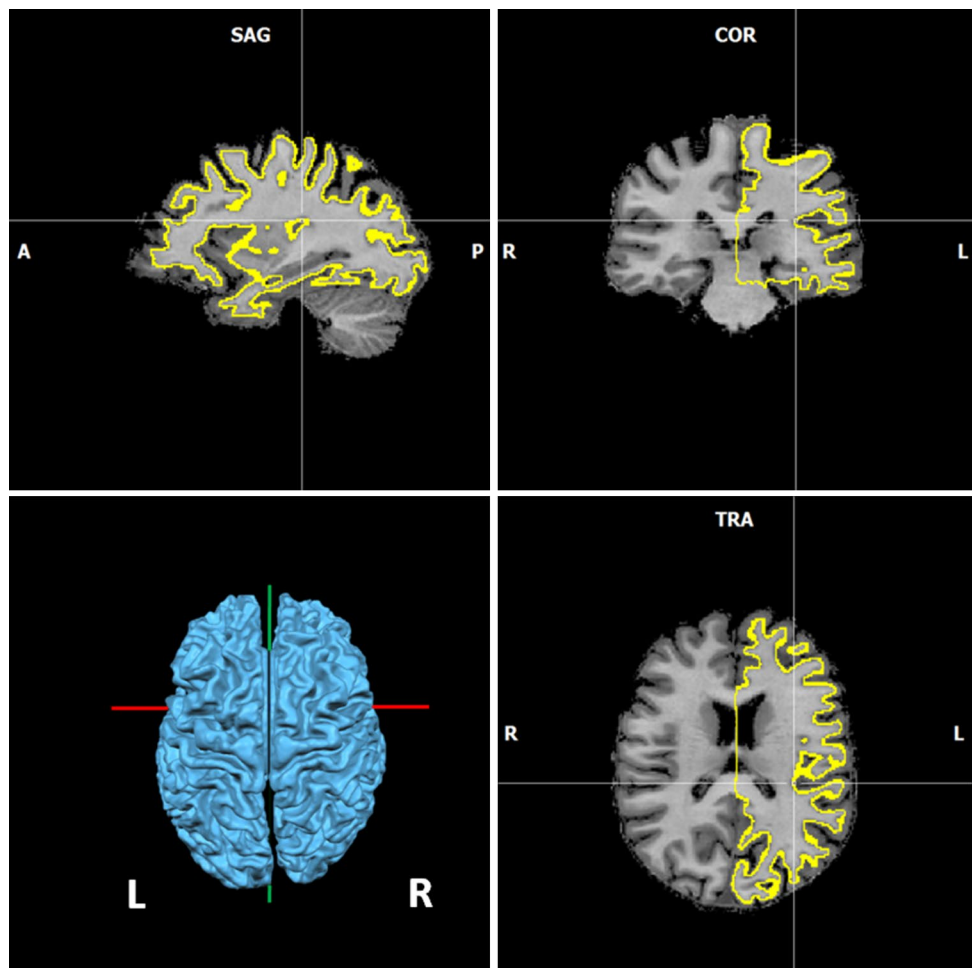
Surface-based segmentation

Following the classification of voxels into cortical GM and subcortical WM, this assignment can be used to construct a tessellated surface following the WM-GM boundary. Here, the contrast and the curvature vary within defined limits, whereas the contrast and curvature of pial surface are more variable. Especially in narrow sulci, the contrast can be grossly diminished by partial-volume averaging and the pial surface that acts as relaxation sink for CSF [34]. In order to circumvent the resulting difficulties, FreeSurfer constructs the pial surface secondary to the subcortical boundary [35].

Because the elementary surfaces and their nodes are interpolated to the pixels, the local precision can be higher than voxel size/image resolution. The interpolated surfaces can be constrained by a Laplacian solution to enforce spherical topology (CLASP, Constrained Laplacian Automated Segmentation by Proximity) [36]. This method is also featured by the Cortical Reconstruction Using Implicit Surface Evolution algorithm (CRUISE) [37] on the MIPAV/JIST platform.

One surface is obtained for each cortical hemisphere, the local parameters “behind the surface”, e.g. cortical

Fig. 5 Surface-based segmentation. Segmentation of the subcortical GM-WM interface of the same subject as in Fig. 3 using BrainVoyager [39]. From these the center of the cortical ribbon is constructed (expanded rendering shown in *lower left*). The voxels containing the tessellated surface are marked in yellow. These are in excellent agreement with the segmentation in Fig. 3, obtained by an independent analysis



thickness, can be mapped onto 2D space [38]. After surface inflation, the pattern of cortical folds, in the form of mean curvature, Gaussian curvature, or average convexity, can be used to characterize geometric differences between populations in the same manner as cortical thickness. Flattening the cortical ribbon can be also exploited for the analysis and display of functional MRI experiments, which is a feature of BrainVoyager (Brain Innovation, Maastricht, Netherlands www.brainvoyager.com). Both FreeSurfer and BrainVoyager use a narrow distribution of WM intensities as a criterion for bias correction. An example of the GM-WM boundary from Brain Voyager [39] is shown in Fig. 5. Since the surface construction is built upon voxel-based segmentation, poor WM-GM contrast (Fig. 6) may influence the position of the boundary.

Cortical thickness

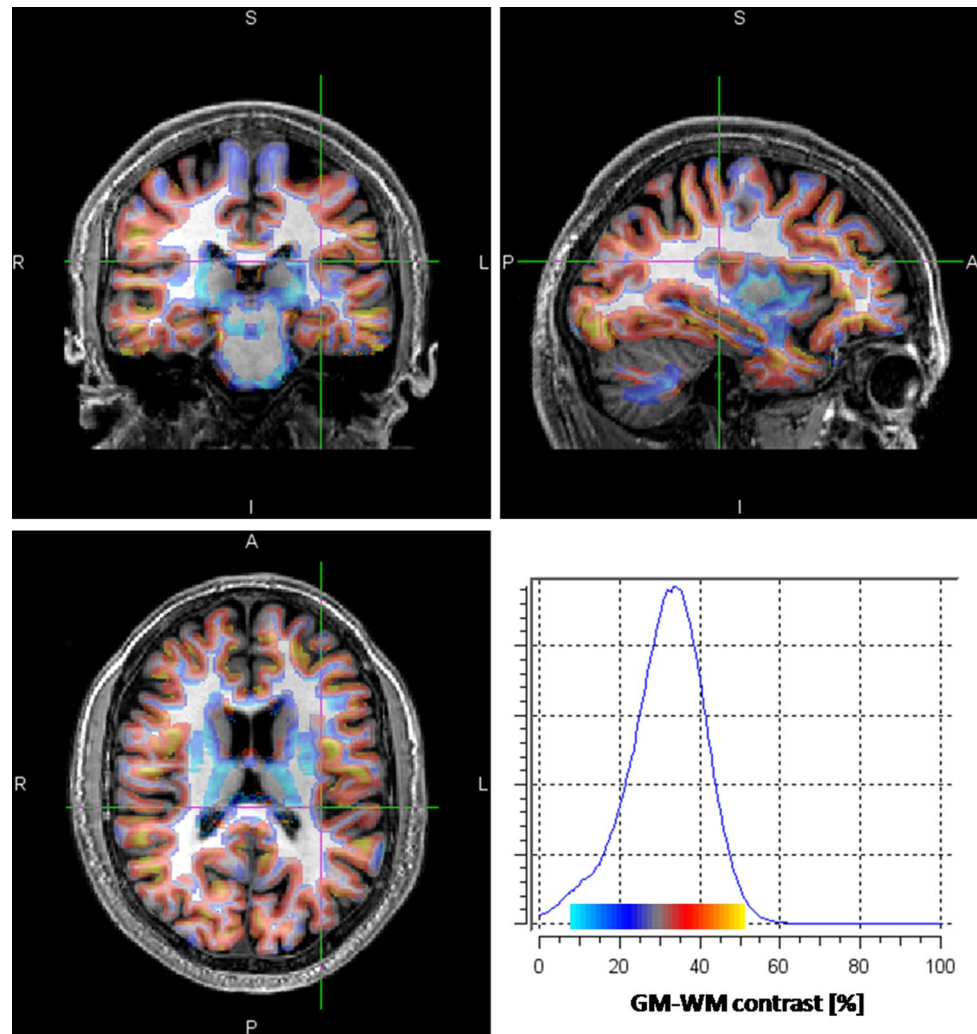
After extracting the subcortical and pial surfaces, there are different ways to derive cortical thickness, e.g., by the nearest distance, a shift perpendicular to the local surface,

or based on local deformation. An SPM-based approach estimates voxel-based cortical thickness (VBCT) from the cortical GM probability [40]. Solving the Laplace equation yields field lines that end orthogonally on the bounding surfaces as first suggested in [36]. Thus, the local estimate for VBCT thickness can be directly submitted to voxel-based statistical analysis. VBCT also yields estimates for deep GM nuclei. Sub-voxel measurements of thickness are possible using sub-sampling and interpolation of the image information. These yield comparable results [41] to surface-based studies of cortical thickness in healthy aging [42]. For 3D Slicer, modules for individual and group-wise analysis of cortical thickness are available, acronymed ARCTIC (Automatic Regional Cortical Thickness) and GAMBIT (Group-wise Automatic Mesh-Based Analysis of Cortical Thickness) under www.nitrc.org/projects [43].

Cortical regions

The term segmentation is also used to denote the assignment of a cortical region (“labeling”) to a pixel in an

Fig. 6 Spatial variation of GM-WM contrast. The local contrast of the MDEFT T1-weighted MRI dataset [10] of Figs. 3 and 5 was calculated over a ribbon along the GM-WM boundary. For each pixel, the neighbouring mean GM and WM intensities were calculated from subspaces of a $5 \times 5 \times 5$ pixel box kernel following discrete assignment. The pseudo-colour scale is shown in the histogram of contrast values $(GM-WM)/(GM+WM) \times 200\%$. Comparison to Figs. 3 and 5 shows that both voxel-based and surface based segmentation are prone to errors in regions of poor contrast (blue) and low intensity gradients. Note that the contrast of the deep grey matter nuclei is on average weaker than that of the cortex



individual brain, implying context-dependent shift in meaning. Roughly, this is done by locally morphing 3D atlases representing the labels to individual anatomy. The application of digital cortical atlases is thus intimately coupled with non-linear registration.

Population-based probabilities for cortical and white matter structures have been assigned to the MNI template, which is widely used as “standard space” for voxel-based statistics. Significant pixel clusters can thus be assigned to the underlying brain regions. There are numerous digital atlases available; selection can be found under fsl.fmrib.ox.ac.uk/fsl/fslwiki/Atlases. By default, FSL provides the Harvard-Oxford atlas of cortical and subcortical structures representing label probabilities on the MNI template. Specialized atlases have been adapted to the infant brain [44], available with iBEAT (Infant Brain Extraction and Analysis Toolbox, www.med.unc.edu/bric/ideagroup/free-software).

It is desirable to perform morphing and assignment on the examined cohorts. Robust, but computationally

expensive tools are now available for this task, e.g. MAB-MIS (Multi-atlas based multi-image segmentation) [45] as 3D Slicer module, or MARS (Multi-atlas robust segmentation) [46]; both available via www.nitrc.org. More detailed information on multi-atlas segmentation is given in dedicated reviews [47, 48].

The hippocampus is of special interest due to its involvement in Alzheimer’s dementia. For example, a dedicated software package for “Automatic Segmentation of Hippocampal Subfields” (ASHS sites.google.com/site/hipposubfields) [49] is using multi-atlas segmentation on a pair of T1-weighted and T2-weighted images, the latter acquired using a protocol tuned for hippocampus imaging.

The substructure of the cerebellum has been addressed only recently. An improved tool for automated topological assignment of cerebellar lobules [50] as compared to “Automatic Classification of Cerebellar Lobules Algorithm using Implicit Multi-boundary evolution” (ACCLAIM) [51] is now available as parts of the TOADS-CRUICE package.

Corpus Callosum

The mid-sagittal cross-section of the corpus callosum is a quantitative anatomical correlated for inter-hemispheric coordination, in particular in conjunction with diffusion-tensor imaging and fiber tracking. Because of the distinct shape and contrast, tool for this 2D problem are long established, e.g. CCseg [52]. A recent implementation is the “yuki” module of the automated registration toolbox (ART, www.nitrc.org/projects/art).

Deep brain nuclei

The problems encountered for segmentation of the deep brain nuclei in the basal ganglia and thalamus differ from those in cortex. In the thalamus, a gradient of axonal content towards the internal capsule results in a smooth transition of contrast rather than a well defined sharp boundary. In addition, a high content of cellular iron renders the T1-weighted signal similar to that of WM. This is most severe in the subthalamic and red nucleus, globus pallidus, and substantia nigra, less so in putamen [9]. Thus, the GM-WM contrast is on average lower than at the cortical boundary (Fig. 6).

The deep brain region thus benefits from optimization of imaging techniques to specifically improve the contrast. The effects of iron can be removed by using magnetization transfer (MT) images where the influence of iron on T1 and T2* has been removed [53]. The effect of axonal content in the thalamus has been addressed by high-resolution multimodal (T1, T2, PD) parameter maps [54]. As mentioned above, the brainstem has been addressed similarly by using PD and MT maps to define classes of monoaminergic GM, reticulated GM, periaqueductal GM, besides WM [31]. The additional information obtained from diffusion tensor imaging and tractography is outside the scope of this review.

The deep brain region is phylogenetically older and thus morphologically much more reproducible than the cortex as seen in the MNI templates (Fig. 4). This favors the application of topologic criteria, as introduced in TOADS [33]. The FSL package features FIRST [55], a Bayesian method to identify the surfaces of number of deep brain nuclei (Fig. 7). These surfaces are rendered as meshes to be visualized and processed with Paraview (www.paraview.org). This mean shifts of the surface between groups or time points can then be displayed by attaching vectors to the surface. It should be noted that prior information obtained from guided manual delineation of MR images (as in FIRST) by necessity suffers from the limited resolution. This can be seen by comparing the shape of the thalamus to

the histology-based 3D Morel atlas of thalamic nuclei [56] (Fig. 7).

Segmentation and quantitative MRI

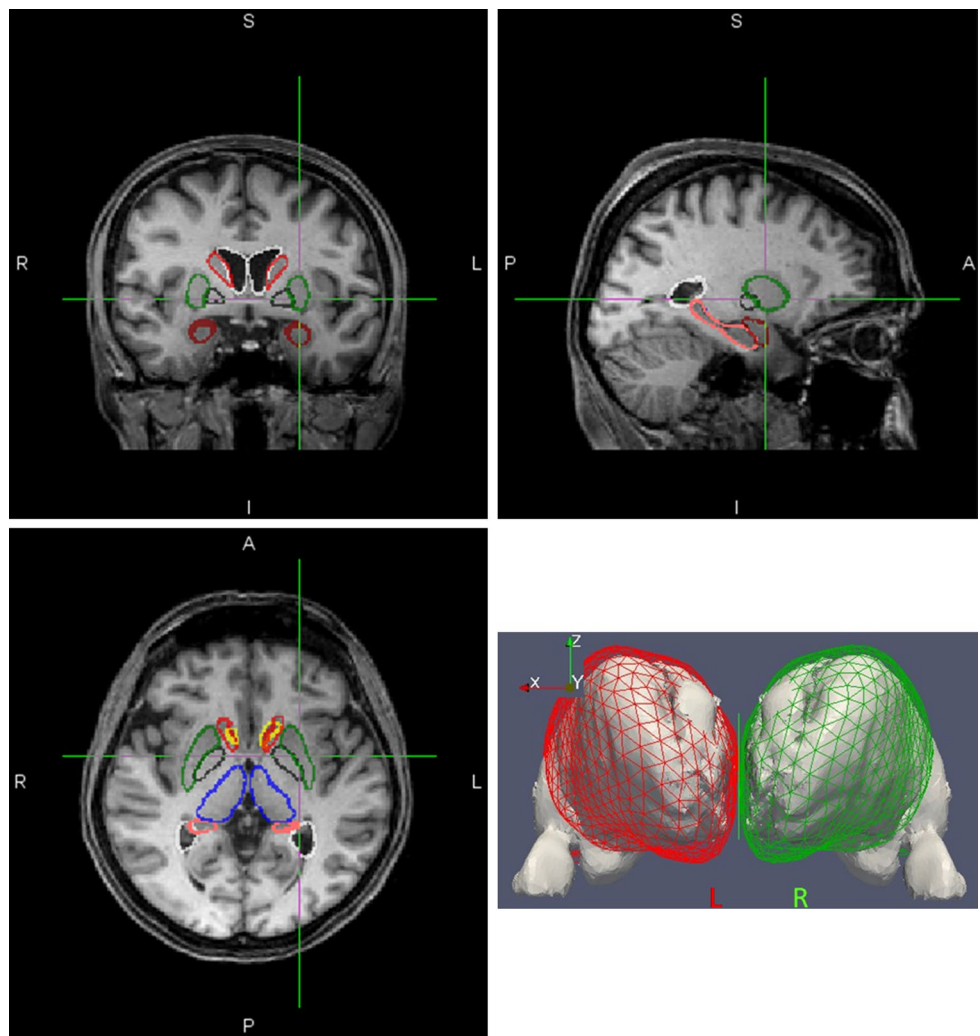
Though brain segmentation started on parameter maps, once the software tools were developed these have been applied back to quantitative MRI (qMRI), that is, the mapping of biophysical parameters in tissues. Since the receive bias field (B_{1-}) cannot be mapped independently from the underlying object and the principle of reciprocity in its simplified form [57] does not hold at field strengths above 2T, the first objective was to use segmentation to obtain unbiased PD maps [58]. In the same way, the flip angle bias field (B_{1+}) can be removed from T1 maps that have been obtained by the variable flip-angle method [59].

A straight forward application of discrete segmentation in qMRI is the use for ROI definition to show the variation of a parameter over the pixels assigned to a tissue. How different partial volumes of each class to a voxel will change the intensity and/or T1 is incompletely described by the Gaussian mixture model (see Fig. 2). Partial volumes can be obtained by modeling the signal equation as sum of fractional signals from three (or more) tissue classes [60, 61]. To solve for the partial volumes repeated measurements at varying flip angles (exceeding the number of classes) and tissue specific values of proton density and T1 are required. The latter can be derived semi-manually from the Gaussian mixture model of individual T1 histograms [60] or semi-manually [61]. Since the criterion of within-class homogeneity is clearly a simplification, local variations will influence the partial volume estimates.

In Fig. 6, a box-kernel was moved along the border of disjunctive GM and WM classes to calculate the local cortical contrast from the mean intensities over the subvolumes. However, the estimates were subject to in a perpendicular gradient caused by neglecting partial volume effects and/or misclassification at the boundary.

A more sublime combination of brain segmentation and qMRI is required when comparing parameter maps over cohorts. Since these show major differences between WM, GM, and CSF, a straight-forward voxel-based comparison cannot differentiate between morphological differences (by volume, extensive) and differences in the parameter (intrinsic tissue property). Voxel-based relaxometry offers a simple processing solution [62]: By weighting the parameter maps by each tissue probability in the Gaussian convolution kernel local GM and WM maps of the parameter can be created, and then submitted to tissue-class specific analysis. A similar approach has been previously applied to maps of fractional anisotropy [63].

Fig. 7 Surface-based segmentation of deep brain nuclei. Outlines of deep brain nuclei segmented using FIRST [55] from the MP-RAGE T1-weighted MRI (as in [14]) of a 64-year-old man. The overlap indicates that the shapes were estimated independently from each other. Caudate nucleus = red; putamen = green, nucleus accumbens = yellow; globus pallidus = black; thalamus = blue; hippocampus = mauve; amygdala = dark red. The outline of the lateral ventricles is shown in white. A comparison of the thalamic surface mesh with a histologically derived thalamus atlas [56] illustrated the simplifications inherent to the MRI-derived FIRST boundaries



Currently the combination of segmentation is being further developed in an endeavor to establish “*in vivo histology*” or “*Brodmann imaging*” based on their underlying biophysical properties that may become discernable especially at ultra-high field strength. For instance, by cortical maps of R1 it is possible to map the myelin-rich primary sensory areas of the cortex at high resolution [64].

Atrophy

In longitudinal cohort studies of disease and healthy aging, the local loss of brain parenchyma is most often detected by VBM of structural MRI. The onset and localization of atrophy is considered a major biomarker in Alzheimer’s and other neurodegenerative diseases. It should be noted that a statistical method such as VBM does not provide quantitative values of volume loss. With the high statistical sensitivity of VBM, local atrophy can be regarded easier to detect than individual changes in total brain volume. Here,

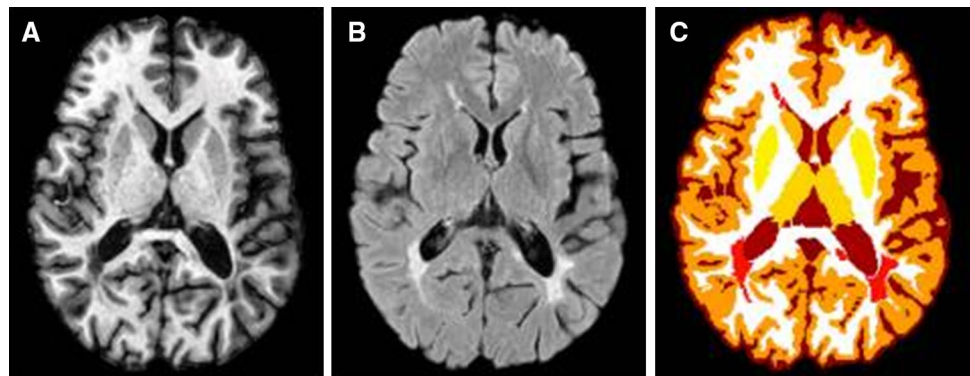
the technical challenge is to achieve sufficient sensitivity to detect atrophy rates of 0.3–0.6 %/year in healthy aging [65] over a feasible time span.

An early method to determine atrophy in individuals from two MRI at two time points was the FSL-based tool SIENA (structural image evaluation, using normalization, of atrophy) [66]. Both datasets are normalized at a halfway position and segmented. From SIENA determines the local perpendicular shift of the brain surface (both pial and ventricular) at corresponding pixels and yields the percentage change of brain atrophy. A comparison of various methods for atrophy measurements in multiple sclerosis is found in [67].

Clinical applications

Both voxel-based and surface-based segmentation methods have been widely used in clinical studies and the field is too large to be covered in this review. The algorithms are

Fig. 8 Segmentation of WM lesions. Multispectral segmentation of MS lesions (red) (c) based on T1-weighted (a) and FLAIR (b) MRI using LesionTOAD. Reproduced with modification from [83]



adjusted to work reliably for typical T1-w MRI datasets of near normal anatomy (see above) and may be readily applied in e.g. psychiatric diseases, epilepsies, and different syndromes and stages of dementia. In epilepsy patients, segmentation was successful in detecting individual epileptogenic sources [68, 69]. In dementia research, the challenge is to detect predictive morphological biomarker against a continuous spectrum of “healthy aging” [70]. Particularly in Alzheimer’s disease, the hippocampus is the target structure for prediction [71, 72].

Segmentation of the basal ganglia is of particular interest to study patients treated with deep brain stimulation (DBS). The LEAD DBS tool has been specifically developed to visualize the DBS electrodes and active regions [73].

Pathologic image contrast, gross morphological deviation, high noise levels and high spatial signal bias, however, may lead to erroneous classification of pixels or structures. Especially methods that heavily rely on priors obtained from healthy subjects (SPM, FIRST) are prone to erroneous results or simply fail in the presence of gross morphological alterations or abnormal contrast. In addition, image artifacts due to poor patient compliance may systematically skew the results. Regarding contrast changes in disease it should be kept in mind that VBM cannot differentiate between altered morphology (due to local volume changes) levels of probability (due to changes of tissue properties). Solutions for automated segmentation in presence of disease thus benefit from taking into account the characteristic pathology.

White matter lesions feature a broad spectrum of shape, location, and contrast. Dedicated segmentation solution thus employ multiple contrasts. As example for a recent solution on the MIPAV platform, Lesion-TOADS [74] combines the intensity information from MPRAGE and FLAIR (fluid-attenuation by inversion recovery) images with statistical and topological atlases to yield the locations and volumes of FLAIR-hyperintense WM lesions (Fig. 8). Within the ABC package, white matter lesions and ventricles are segmented via postprocessing using level-set segmentation [75]. The module for white matter

lesion segmentation on the 3D Slicer platform (www.nitrc.org/projects/hammerwml) uses pattern recognition on T1-weighted, T2-weighted, PD-weighted, and FLAIR MR brain images [76]. The Wisconsin White Matter Hyperintensities Segmentation Toolbox (W2MHS www.nitrc.org/projects/w2mhs) is an open source MATLAB toolbox dedicated to Alzheimer’s and aging-related neurological disorders [77]. In multiple sclerosis (MS), lesion types range from “dirty white matter” over “black holes” to “burnt out” lesions resembling CSF. The use of segmentation in MS is discussed in a dedicated review [78].

An early solution for automated segmentation of brain tumours is 4D-PARSeR (Pathological Anatomy Regression via Segmentation and Registration), available as a module for the 3D Slicer platform [79]. More recent, Brain Tumor Image Analysis (BraTumIA www.nitrc.org/projects/bratumia) performs segmentation of healthy and tumor tissues by from multispectral MRI (pre-/post contrast T1-weighted, T2-weighted, and FLAIR) identifying necrotic core, edema, non-enhancing tumor, and enhancing tumor. The authors provide an exhaustive review of brain tumour segmentation [80].

If longitudinal (4D) data is available to address dynamics, morphological consistency can be exploited to support the segmentation. This principle has been applied to infants when the cortical contrast undergoes stark changes due to myelination [81] or after traumatic brain injury [82].

Segmentation is the prerequisite to quantitatively assess morphological changes in disease and healthy aging. The trend is to examine ever larger patients and control cohorts at multiple centers organized by consortiums and to making data available by public databases. The need for consistent evaluation has lead to tool for “pipelining” data through a multi-level automated processing. The Java Image Science Toolkit (JIST) provides a native Java-based imaging processing environment similar to the ITK/VTK paradigm. Initially developed as an extension to MIPAV (CIT, NIH, Bethesda, MD, USA), the JIST processing infrastructure provides automated GUI generation for application plugins, graphical layout tools, and command line interfaces. It

is open to development and used in the “MR Connectome Automated Pipeline” and by several of the packages mentioned above (TOADS CBS High-Res Tools).

Concluding remarks

Segmentation of human brain using structural MRI is a key step in imaging neuroscience. The methods have undergone a rapid development in the past 20 years. They can now be considered mature and are widely available, even for detection of lesions or neoplasms. This non-technical review aims at providing an overview and basic understanding of the most common techniques.

Compliance with ethical standards

All procedures performed in studies involving human participants were accordance with the ethical standards of the institutional research committee and with the 1964 Helsinki declaration and its later amendments or comparable ethical standards.

Conflict of interest The author has no conflicts of interest to declare.

Funding The author is supported by the Swedish Research Council.

References

1. Lim KO, Pfefferbaum A (1989) Segmentation of MR brain images into cerebrospinal fluid spaces, white and gray matter. *J Comput Assist Tomogr* 13:588–593
2. Ashburner J (2012) SPM: a history. *Neuroimage* 62:791–800
3. Lucas B, Bogovic J, Carass A, Bazin P-L, Prince J, Pham D, Landman B (2010) The Java image science toolkit (JIST) for rapid prototyping and publishing of neuroimaging software. *Neuroinformatics* 18:5–17
4. Fedorov A, Beichel R, Kalpathy-Cramer J, Finet J, Fillion-Robin J-C, Pujol S, Bauer C, Jennings D, Fennessy F, Sonka M, Buatti J, Aylward SR, Miller JV, Pieper S, Kikinis R (2012) 3D Slicer as an image computing platform for the quantitative imaging network. *Magn Reson Imaging* 30(9):1323–1341
5. Warfield SK, Zou KH, Wells WM (2004) Simultaneous truth and performance level estimation (STAPLE): an algorithm for the validation of image segmentation. *IEEE Trans Med Imaging* 23(7):903–921
6. Koenig SH, Brown RD 3rd, Spiller M, Lundbom N (1990) Relaxometry of brain: why white matter appears bright in MRI. *Magn Reson Med* 14(3):482–495
7. Kamman RL, Go KG, Brouwer W, Berendsen HJ (1988) Nuclear magnetic resonance relaxation in experimental brain edema: effects of water concentration, protein concentration, and temperature. *Magn Reson Med* 6(3):265–274
8. Gelman N, Gorell JM, Barker PB, Savage RM, Spickler EM, Windham JP, Knight RA (1999) MR imaging of human brain at 3.0 T: preliminary report on transverse relaxation rates and relation to estimated iron content. *Radiology* 210(3):759–767
9. Gelman N, Ewing JR, Gorell JM, Spickler EM, Solomon EG (2001) Interregional variation of longitudinal relaxation rates in human brain at 3.0 T: relation to estimated iron and water contents. *Magn Reson Med* 45(1):71–79
10. Hallgren B, Sourander P (1958) The effect of age on the non-haem iron in the human brain. *J Neurochem* 3(1):41–51
11. Helms G, Kallenberg K, Dechent P (2006) A contrast-driven approach to intracranial segmentation using a combination of T2- and T1-weighted 3D MRI datasets. *J Magn Reson Imaging* 24(4):790–795
12. Deichmann R, Good CD, Josephs O, Ashburner J, Turner R (2000) Optimization of 3-D MP-RAGE sequences for structural brain imaging. *Neuroimage* 12:112–127
13. Deichmann R, Schwarzbauer C, Turner R (2004) Optimisation of the 3D MDEFT sequence for anatomical brain imaging: technical implications at 1.5 and 3 T. *NeuroImage* 21:757–767
14. Jack CJ, Bernstein M, Fox N, Thompson P, Alexander G, Harvey D, Borowski B, Britson P, Whitwell J, Ward C, Dale A, Felmlee J, Gunter J, Hill D, Killiany R, Schuff N, Fox-Bosetti S, Lin C, Studholme C, DeCarli C, Krueger G, Ward H, Metzger G, Scott K, Mallozzi R, Blezek D, Levy J, Debbs J, Fleisher A, Albert M, Green R, Bartzokis G, Glover G, Mugler J, Weiner M (2008) The Alzheimer’s disease neuroimaging initiative (ADNI): MRI methods. *J Magn Reson Imaging* 27(4):685–691
15. Alfano B, Brunetti A, Covelli EM, Quarantelli M, Panico MR, Ciarmiello A, Salvatore M (1997) Unsupervised, automated segmentation of the normal brain using a multispectral relaxometric magnetic resonance approach. *Magn Reson Med* 37(1):84–93
16. Sled JG, Zijdenbos AP, Evans AC (1998) A non-parametric method for automatic correction of intensity non-uniformity in MRI. *IEEE Trans Med Imag* 17:87–97
17. Tustison NJ, Avants BB, Cook PA, Zheng Y, Egan A, Yushkevich PA, Gee JC (2010) N4ITK: improved N3 bias correction. *IEEE Trans Med Imag* 29(6):1310–1320
18. Zhang Y, Brady M, Smith S (2001) Segmentation of brain MR images through a hidden Markov random field model and the expectation–maximization algorithm. *IEEE Trans Med Imaging* 20(1):45–57
19. Smith SM (2002) Fast robust automated brain extraction. *Hum Brain Mapp* 17(3):143–155
20. Iglesias JE, Liu CY, Thompson PM, Tu Z (2011) Robust brain extraction across datasets and comparison with publicly available methods. *IEEE Trans Med Imaging* 30:1617–1634
21. Ségonne F, Dale AM, Busa E, Glessner M, Salat D, Hahn HK, Fischl B (2004) A hybrid approach to the skull stripping problem in MRI. *Neuroimage* 22(3):1060–1075
22. Carass A, Cuzzocreo J, Wheeler MB, Bazin PL, Resnick SM, Prince JL (2011) Simple paradigm for extra-cerebral tissue removal: algorithm and analysis. *Neuroimage* 56(4):1982–1992
23. Mikheev A, Neovsky G, Govindan S, Grossman R, Rusinek HJ (2008) Fully automatic segmentation of the brain from T1-weighted MRI using Bridge Burner algorithm. *J Magn Reson Imaging* 27(6):1235–1241
24. Woolrich MW, Jbabdi S, Patenaude B, Chappell M, Makni S, Behrens T, Beckmann C, Jenkinson M, Smith SM (2009) Bayesian analysis of neuroimaging data in FSL. *Neuroimage* 45:S173–S186
25. Ashburner J, Friston K (1997) Multimodal image coregistration and partitioning—a unified framework. *Neuroimage* 6(3):209–217
26. Ashburner J, Friston KJ (2005) Unified segmentation. *Neuroimage* 26(3):839–851
27. Evans AC, Kamber M, Collins DL, Macdonald D (1994) An MRI-based probabilistic atlas of neuroanatomy. In: Shorvon S, Fish D, Andermann F, Bydder GM, Stefan H (eds) Magnetic resonance scanning and epilepsy, NATO ASI series A, life sciences, vol 264. Plenum, New York, pp 263–274

28. van Leemput K, Maes F, Vandermeulen D, Suetens P (1999) Automated model-based tissue classification of MR images of the brain. *IEEE Trans Med Imaging* 18(10):897–908
29. Draganski B, Gaser C, Busch V, Schuierer G, Bogdahn U, May A (2004) Neuroplasticity: changes in grey matter induced by training. *Nature* 427(6972):311–312
30. Focke NK, Helms G, Kaspar S, Diederich C, Tóth V, Dechen P, Mohr A, Paulus W (2011) Multi-site voxel-based morphometry—not quite there yet. *Neuroimage* 56(3):1164–1170
31. Lambert C, Lutti A, Helms G, Frackowiak R, Ashburner J (2013) Multiparametric brainstem segmentation using a modified multivariate mixture of gaussians. *Neuroimage Clin* 16(2):684–694
32. Bazin P-L, Pham D (2007) Topology correction of segmented medical images using a fast marching algorithm. *Comput Methods Programs Biomed* 88:182–190
33. Bazin P-L, Pham D (2008) Homeomorphic brain image segmentation with topological and statistical atlases. *Med Image Anal* 12:616–625
34. Brownstein KR, Tarr CE (1977) Spin-lattice relaxation in a system governed by diffusion. *J Magn Reson* 26:17–24
35. Fischl B, Dale AM (2000) Measuring the thickness of the human cerebral cortex from magnetic resonance images. *Proc Natl Acad Sci USA* 97(20):11050–11055
36. Kim JS, Singh V, Lee JK, Lerch J, Ad-Dab'bagh Y, MacDonald D, Lee JM, Kim SI, Evans AC (2005) Automated 3-D extraction and evaluation of the inner and outer cortical surfaces using a Laplacian map and partial volume effect classification. *Neuroimage* 27(1):210–221
37. Han X, Pham D, Tosun D, Rettmann M, Xu C, Prince J (2004) CRUISE: cortical reconstruction using implicit surface evolution. *Neuroimage* 23:997–1012
38. Dale AM, Fischl B, Sereno MI (1999) Cortical surface-based analysis I. Segmentation and surface reconstruction. *Neuroimage* 9:179–194
39. Kriegeskorte N, Goebel R (2001) An efficient algorithm for topologically correct segmentation of the cortical sheet in anatomical MR volumes. *NeuroImage* 14:329–346
40. Hutton C, De Vita E, Ashburner J, Deichmann R, Turner R (2008) Voxel-based cortical thickness measurements in MRI. *Neuroimage* 40(4):1701–1710
41. Hutton C, Draganski B, Ashburner J, Weiskopf N (2009) A comparison between voxel-based cortical thickness and voxel-based morphometry in normal aging. *Neuroimage* 48(2):371–380
42. Salat DH, Buckner RL, Snyder AZ, Greve DN, Desikan RSR, Busa E, Morris JC, Dale AM, Fischl B (2004) Thinning of the cerebral cortex in aging. *Cereb Cortex* 14(7):721–730
43. Vachet C, Hazlett HC, Niethammer M, Oguz I, Cates J, Whitaker R, Piven J, Styner M (2011) Group-wise automatic mesh-based analysis of cortical thickness. In: Presented at the medical imaging 2011: image processing 7962(1):796227
44. Shi F, Yap P-T, Wu G, Jia H, Gilmore JH, Lin W, Shen D (2011) Infant brain atlases from neonates to 1- and 2-year-olds. *PLoS One* 6(4):e18746
45. Jia H, Yap PT, Shen D (2012) Iterative multi-atlas-based multi-image segmentation with tree-based registration. *Neuroimage* 59(1):422–430
46. Wu G, Wang Q, Zhang D, Nie F, Huang H, Shen D (2014) A generative probability model of joint label fusion for multi-atlas based brain segmentation. *Med Image Anal* 18(6):881–890
47. Iglesias JE, Sabuncu MR (2015) Multi-atlas segmentation of biomedical images: a survey. *Med Imag Anal* 24(1):205–219
48. Cabezas M, Oliver A, Lladó X, Freixenet J, Cuadra MB (2011) A review of atlas-based segmentation for magnetic resonance brain images. *Comput Methods Programs Biomed* 104(3):e158–e177. doi:10.1016/j.cmpb.2011.07.015
49. Yushkevich PA, Pluta J, Wang H, Ding SL, Xie L, Gertje E, Mancuso L, Kliot D, Das SR, Wolk DA (2014) Automated volumetry and regional thickness analysis of hippocampal subfields and medial temporal cortical structures in mild cognitive impairment. *Hum Brain Mapp* 36(1):258–287
50. Yang Z, Y C, Bogovic JA, Carass A, Jedynak BM, Ying SH, Prince JL (2015) Automated cerebellar lobule segmentation with application to cerebellar structural analysis in cerebellar disease. *Neuroimage* doi:10.1016/j.neuroimage.2015.09.032. [Epub ahead of print]
51. Bogovic JA, Bazin PL, Ying SH, Prince JL (2013) Automated segmentation of the cerebellar lobules using boundary specific classification and evolution. *Inf Process Med Imaging* 23:62–73
52. Vachet C, Yvernaud B, Bhatt K, Smith RG, Gerig G, Hazlett HC, Styner M (2012) Automatic corpus callosum segmentation using a deformable active Fourier contour model. *Proc SPIE Int Soc Opt Eng* 8317:831707. doi:10.1117/12.911504
53. Helms G, Draganski B, Frackowiak R, Ashburner J, Weiskopf N (2009) Reliable segmentation of deep brain grey matter structures using magnetization transfer (MT) parameter maps. *Neuroimage* 47:194–198
54. Deoni SC, Rutt BK, Parrent AG, Peters TM (2007) Segmentation of thalamic nuclei using a modified k-means clustering algorithm and high-resolution quantitative magnetic resonance imaging at 1.5 T. *Neuroimage* 34:117–126
55. Patenaude B, Smith SM, Kennedy D, Jenkinson M (2011) A Bayesian model of shape and appearance for subcortical brain. *Neuroimage* 56(3):907–922
56. Krauth A, Blanc R, Poveda A, Jeanmonod D, Morel A, Székely G (2010) A mean three-dimensional atlas of the human thalamus: generation from multiple histological data. *Neuroimage* 49(3):2053–2062
57. Holt DI (2000) The principle of reciprocity in signal strength calculations—a mathematical guide. *Concepts Magn Reson* 14(4):173–187
58. Volz S, Nöth U, Deichmann R (2012) Correction of systematic errors in quantitative proton density mapping. *Magn Reson Med* 68(1):74–85
59. Weiskopf N, Lutti A, Helms G, Novak M, Ashburner J, Hutton C (2011) Unified segmentation based correction of R1 brain maps for RF transmit field inhomogeneities (UNICORT). *Neuroimage* 54(3):2116–2124
60. Shin W, Geng X, Gu H, Zhan W, Zou Q, Yang Y (2010) Automated brain tissue segmentation based on fractional signal mapping from inversion recovery look-locker acquisition. *Neuroimage* 52:1347–1354
61. Ahlgren A, Wirestam R, Ståhlberg F, Knutsson L (2014) Automatic brain segmentation using fractional signal modeling of a multiple flip angle, spoiled gradient-recalled echo acquisition. *Magn Reson Mater Phy* 27:551–565
62. Draganski B, Ashburner J, Hutton C, Kherif F, Frackowiak RS, Helms G, Weiskopf N (2011) Regional specificity of MRI contrast parameter changes in normal ageing revealed by voxel-based quantification (VBQ). *Neuroimage* 55(4):1423–1434
63. Càmara E, Bodammer N, Rodríguez-Fornells A, Tempelmann C (2007) Age-related water diffusion changes in human brain: a voxel-based approach. *Neuroimage* 34:1588–1599
64. Dick F, Tierney AT, Lutti A, Josephs O, Sereno MI, Weiskopf N (2012) In vivo functional and myeloarchitectonic mapping of human primary auditory areas. *J Neurosci* 32(46):16095–16105
65. Miller DH, Barkhof F, Frank JA, Parker GJM, Thompson AJ (2002) Measurement of atrophy in multiple sclerosis: pathological basis, methodological aspects and clinical relevance. *Brain* 125:1676–1692
66. Smith SM, Zhang Y, Jenkinson M, Chen J, Matthews PM, Federico A, De Stefano N (2002) Accurate, robust, and automated

- longitudinal and cross-sectional brain change analysis. *Neuroimage* 17:479–489
67. Durand-Dubief F, Belaroussi B, Armpach JP, Dufour M, Roggerone S, Vukusic S, Hannoun S, Sapay-Marinier D, Confavreux C, Cotton F (2012) Reliability of longitudinal brain volume loss measurements between 2 sites in patients with multiple sclerosis: comparison of 7 quantification techniques. *AJNR Am J Neuroradiol* 33(10):1918–1924
68. Bernasconi A, Bernasconi N, Bernhardt BC, Schrader D (2011) Advances in MRI for ‘cryptogenic’ epilepsies. *Nat Rev Neurol* 7(2):99–108
69. Martin P, Bender B, Focke NK (2015) Post-processing of structural MRI for individualized diagnostics. *Quant Imaging Med Surg* 5(2):188–203
70. Teipel SJ, Grothe M, Lista S, Toschi N, Garaci FG, Hampel H (2013) Relevance of magnetic resonance imaging for early detection and diagnosis of Alzheimer disease. *Med Clin North Am* 97(3):399–424
71. Braskie MN, Thompson PM (2014) A focus on structural brain imaging in the Alzheimer’s disease neuroimaging initiative. *Biol Psychiatry* 75(7):527–533
72. Jack CR Jr, Barkhof F, Bernstein MA, Cantillon M, Cole PE, DeCarli C, Dubois B, Duchesne S, Fox NC, Frisoni GB, Hampel H, Hill DLG, Johnson K, Mangin J-F, Scheltens P, Schwarz AJ, Sperling R, Suhy J, Thompson PM, Weiner M, Foster NL (2011) Steps to standardization and validation of hippocampal volumetry as a biomarker in clinical trials and diagnostic criteria for Alzheimer’s disease. *Alzheimers Dement* 7(4):474–485
73. Horn A, Kühn AA (2014) Lead-DBS: a toolbox for deep brain stimulation electrode localizations and visualizations. *Neuroimage* 107:127–135
74. Shiee N, Bazin P-L, Ozturk A, Reich DS, Calabresi PA, Pham DL (2010) A topology-preserving approach to the segmentation of brain images with multiple sclerosis lesions. *Neuroimage* 49:1524–1535
75. Prastawa M, Gerig G (2008) Brain Lesion Segmentation through physical model estimation. *Int Symp Vis Comput (ISVC) Lect Notes Comput Sci (LNCS)* 5358:562–571
76. Lao Z, Shen D, Liu D, Jawad AF, Melhem ER, Launer LJ, Bryan NR, Davatzikos C (2008) Computer-assisted segmentation of white matter lesions in 3D MR images using pattern recognition. *Acad Radiol* 15(3):300–313
77. Ithapu V, Singh V, Lindner C, Austin BP, Hinrichs C, Carlsson CM, Bendlin BB, Johnson SC (2014) Extracting and summarizing white matter hyperintensities using supervised segmentation methods in Alzheimer’s disease risk and aging studies. *Hum Brain Mapp*. doi:[10.1002/hbm.22472](https://doi.org/10.1002/hbm.22472)
78. García-Lorenzo D, Francis S, Narayanan S, Arnold DL, Collins DL (2013) Review of automatic segmentation methods of multiple sclerosis white matter lesions on conventional magnetic resonance imaging. *Med Image Anal* 17(1):1–18
79. Moon N, Bullitt E, van Leemput K, Gerig G (2002) Automatic brain and tumor segmentation. In: Proceedings of MICCAI ’02, Springer LNCS 2488, 09/2002
80. Bauer S, Wiest R, Nolte LP, Reyes M (2013) A survey of MRI-based medical image analysis for brain tumor studies. *Phys Med Biol* 58(13):R97–R129
81. Wang L, Shi F, Yap P-T, Lin W, Gilmore JH, Shen D (2013) Longitudinally guided level sets for consistent tissue segmentation of neonates. *Hum Brain Mapp* 34:956–972
82. Wang B, Prastawa M, Irimia A, Chambers MC, Sadeghi N, Vespa PM, van Horn JD, Gerig G (2013) Analyzing imaging biomarkers for traumatic brain injury using 4D modeling of longitudinal MRI. *Proc IEEE Int Symp Biomed Imaging* 2013:1392–1395
83. Shiee N, Bazin P-L, Zackowski KM, Farrell SK, Harrison DM, Newsome SD, Ratchford JN, Caffo BS, Calabresi PA, Pham DL, Reich DS (2012) Revisiting brain atrophy and its relationship to disability in multiple sclerosis. *PLoS One* 7(5):e37049. doi:[10.1371/journal.pone.0037049](https://doi.org/10.1371/journal.pone.0037049)